Research Article | Vol. 28, No. 4 / 17 February 2020 / Optics Express 4938
Optics EXPRESS

High-Q suspended optical resonators in 3C silicon carbide obtained by thermal annealing

KEITH POWELL,[1,2] AMIRHASSAN SHAMS-ANSARI,[2] SMIT DESAI,[1] MITCHELL AUSTIN,[1] JIANGDONG DENG,[3] NEIL SINCLAIR,[2,4] MARKO LONČAR,[2,5] AND XIAOKE YI[1,6]

[1]*School of Electrical and Information Engineering, Institute of Photonics and Optical Science, The University of Sydney, NSW 2006, Australia*
[2]*John A. Paulson School of Engineering and Applied Sciences, Harvard University, 29 Oxford Street, Cambridge, MA 02138, USA*
[3]*Center for Nanoscale Systems, Harvard University, Cambridge, MA 02138, USA*
[4]*Division of Physics, Mathematics and Astronomy, and Alliance for Quantum Technologies (AQT), California Institute of Technology, 1200 East California Boulevard, Pasadena, CA 91125, USA*
[5]*loncar@seas.harvard.edu*
[6]*xiaoke.yi@sydney.edu.au*

Abstract: We fabricate suspended single-mode optical waveguides and ring resonators in 3C silicon carbide (SiC) that operate at telecommunication wavelength, and leverage post-fabrication thermal annealing to minimize optical propagation losses. Annealed optical resonators yield quality factors of over 41,000, which corresponds to a propagation loss of 7 dB/cm, and is a significant improvement over the 24 dB/cm in the case of the non-annealed chip. This improvement is attributed to the enhancement of SiC crystallinity and a significant reduction of waveguide surface roughness, from 2.4 nm to below 1.7 nm. The latter is attributed to surface layer oxide growth during the annealing step. We confirm that the thermo-optic coefficient, an important parameter governing high-power and temperature-dependent performance of SiC, does not vary with annealing and is comparable to that of bulk SiC. Our annealing-based approach, which is especially suitable for suspended structures, offers a straightforward way to realize high-performance 3C-SiC integrated circuits.

1. Introduction

An important goal in the development of integrated photonics is the possibility to achieve integration of efficient functionality between multiple components on a monolithic platform [1]. Applications such as high-speed modulation and efficient frequency conversion together with CMOS compatibility and scalability can create numerous opportunities for integrated photonics [1,2].

Cubic silicon carbide (3C-SiC) has been gaining momentum as a platform to realize many optical functionalities due to its diverse properties. For example, the large second order ($\chi 2$) susceptibility of 34 pm/V [3] and high third order non-linearity ($\chi 3$) [4,5] allows for electro-optic applications and efficient non-linear optical frequency conversion [6]. SiC is a CMOS compatible material [7,8] with several favorable properties such as a wide band-gap [9], absence of two photon absorption at telecom wavelengths [10], high chemical resistance in harsh environments [11], high optical power handling [12], low thermo-optic coefficient [13], high thermal conductivity and large Young's modulus of 450 GPa [14]. Moreover, various polytypes of SiC are efficient quantum emitters both optically pumped and electrically driven in visible and telecom wavelengths [6,15–20], making SiC ideal for a wide range of applications in integrated optics. Within this frame, 3C-SiC is the only one that can be grown on a host substrate (Si) with the option to grow SiC to an exact thickness required for the targeted application, which

#381601 https://doi.org/10.1364/OE.381601
Journal © 2020 Received 7 Nov 2019; revised 3 Jan 2020; accepted 27 Jan 2020; published 7 Feb 2020

Optics EXPRESS

features the advantage of scalability and compatibility with electronic devices [21]. In addition the isotropic crystal structure and symmetric electro-optic tensor make 3C-SiC attractive for birefringent free electro-optic devices [22,23] and allow for novel quasi-phase matching schemes for efficient second order non-linear processes [24,25].

Recent work on the SiC on-insulator (SiCOI) platforms such as 3C and 4H SiC have garnered much interest [26–28]. In 3C-SiCOI a flip, bond, etch and polish method was developed to bond 3C-SiC onto an insulating wafer of thermal SiO_2 on Si [26]. With this technique the stacking faults and anti-phase boundaries at the SiC-Si interface were removed in the chemical mechanical polishing (CMP) step resulting in a propagation loss of 3 dB/cm [27].

Suspended SiC photonic structures, such as waveguides, micro-disks [29–31] and photonic crystal cavities [32–36] are of interest for opto-mechanical experiments [37], accelerometry, large-surface applications such as sensing, coupling of phonons to quantum emitters [38,39], and control of these emitters using surface acoustic waves [40]. Suspended SiC structures fabricated on standard SiC on Si substrates are compatible with high temperature thermal annealing [41,42]. These are useful for increasing the crystal purity for lowered scattering or absorption losses from imperfect material growth, oxidation-smoothing of sidewalls with oxygen annealing or implantation of ions such as vanadium or rare earths [43].

Up to now, suspended 3C-SiC ring resonators feature optical quality (Q) factors in the range of 11000-24,000 [34,44], where the latest results show waveguides featuring propagation losses of 21 dB/cm using 1550 nm light [34]. Although this is an impressive performance for a hard-to-etch polycrystalline material so far, these propagation losses inhibit suspended 3C-SiC devices for integrated photonic applications. Wet-oxidization [27] and thermal annealing [29] have been applied on 4H SiCOI microrings and 3C-SiC microdisks respectively to improve their Q-factors, however to date there has no report on dry oxidization of 3C-SiC optical structures in an oxygen atmosphere. In this paper, we show that post fabrication thermal annealing and a new etching process can significantly reduce waveguide loss in these types of structures. A root-mean-squared (RMS) roughness of 2.4 nm is achieved on top of the fabricated waveguide after wafer thinning and etching, which is further reduced to 1.7 nm after annealing. Our results show a reduction in loss from 24 dB/cm to 7 dB/cm at 1550 nm by annealing the waveguides in a high temperature oxygen atmosphere corresponding to an intrinsic (Q) factor of over 41,000. We investigate the mechanisms for annealing-induced loss reduction by x-ray diffraction (XRD), x-ray photoelectron spectroscopy (XPS), atomic force microscopy (AFM), and scanning electron microscopy (SEM) analysis. Our measurements suggest loss reduction occurs from the combination of reduction in surface roughness and enlargement of crystal grains. These effects could also aid in the reduction of crystal defect density such as stacking faults and anti-phase boundaries at the SiC-Si interface that have been shown to occur [45]. Specifically, polycrystalline grains are enlarged as indicated by a 50% reduction in full width half maximum (FWHM) of 3C-SiC intensities of the XRD scans, showing an increase in crystallinity. The combination of the aforementioned effects result in a large reduction in linear propagation loss. Additionally, we perform accurate measurement of the thermo-optic coefficient of 5.7×10^{-5}/K in the fabricated 3C-SiC waveguides before and after annealing and confirm that our annealing technique does not alter this property.

2. Fabrication method

The devices are fabricated using an etch and undercut method based on the work of Martini *et al*. [34]. Our modified process employs a new anisotropic as well as isotropic etch followed by thermal annealing as depicted in Fig. 1. A 3.5 μm-thick film of epitaxially-grown 3C-SiC on a 4 inch-diameter silicon wafer (NOVASIC) serves as a handle for the fabricated structures. First, the SiC layer is thinned down to 450 nm using a fluorine-based inductively coupled plasma reactive ion etching (ICP-RIE) process that is optimized for low surface roughness at a rate of ~100 nm/min. Rib waveguides are then patterned on the device layer using a negative-tone

Optics EXPRESS

electron-beam resist of hydrogen silsesquioxane (HSQ), (FOX-16, Dow Corning), spun multiple times with heat treatment between each spin to reach the desired thickness of ~2 µm. The thickness of the resist is chosen to allow sufficient dry etching time for a selectivity of 1:4 SiC:HSQ based on our etch recipe, and circumvents the use of a metal hard mask which typically result in higher sidewall roughness. Our resist is exposed by electron beam lithography (EBL) and the exposed resist is developed using a solution of 25% tetramethylammonium hydroxide (TMAH) at room temperature. The cross-section of the pattern is depicted in Fig. 1(a). Next the same etch recipe is used to define the patterned structures into the device layer (Fig. 1(b)), with the remaining HSQ removed by hydrofluoric acid (HF). A second EBL and etching step is required to fabricate partially etched vertical grating couplers (VGCs). These are chosen over fully etched VGCs to prevent cracking of the SiC thin film after undercut. As shown in Fig. 1(c) polymethyl methacrylate (PMMA) (950 series A9, MicroChem) positive-tone resist is used as an etch mask for the VGCs and patterned with EBL and developed in a 1:3 mixture of methyl isobutyl ketone (MIBK) and isopropanol. After the ICP-RIE process, the remaining PMMA in Fig. 1(d) is removed using N-Methyl-2-Pyrrolidone (NMP).

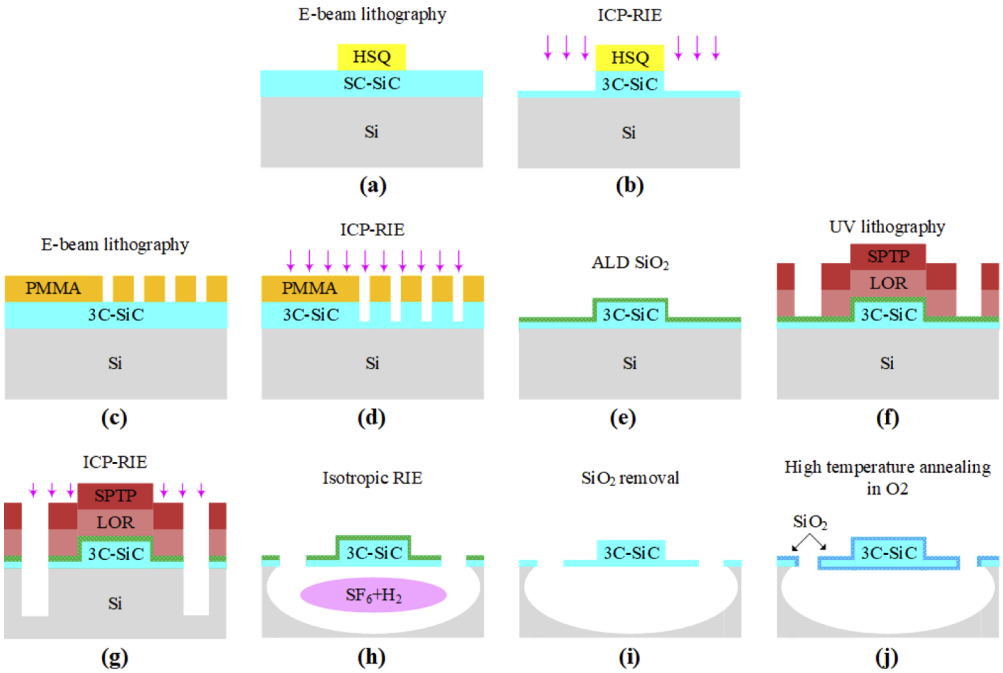

Fig. 1. Schematic representation of the device fabrication process, (a)-(b) rib waveguide etch, (c)-(d) shallow etching of vertical grating couplers, (e)-(j) waveguide undercut process (k) thermal annealing in O_2 for sidewall smoothing and crystal defect reduction.

A protective layer of SiO_2 is deposited using atomic layer deposition (ALD) to prevent surface damage to the underlying SiC during the undercut etch (Fig. 1(e)). Next, perforations for the undercut that surround the waveguides are patterned using photolithography. A bilayer stack of lift-off resist (LOR) and Shipley positive-tone photoresist (SPTP) are spin coated onto the substrate at a thickness of 300 nm and 2 µm respectively (Fig. 1(f)). The LOR facilitates lift-off of the hard Shipley resist while providing additional etch resistance. The perforations are first anisotropically etched (Fig. 1(h)) using the aforementioned etch recipe with the remaining resist removed using NMP and piranha solution (1:3 ratio of hydrogen peroxide and sulfuric acid). Next, we perform an isotropic ICP-RIE process to complete the undercut. We develop an alternative

Optics EXPRESS

etch recipe to that based on XeF_2 (conventional) due to the availability of process gases and compatibility with standard ICP-RIE chambers. Specifically we use a combination of SF_6 and H_2 in the chamber at high pressure with zero RF bias (Fig. 1(i)). This method achieves high etch rates of ~2 μm/s. Following this step, the protective SiO_2 layer is removed by HF (Fig. 1(j)) and then the substrate is cleaned in piranha solution. The SiC waveguides are then annealed in O_2 atmosphere at 1100°C for 2 hours (Fig. 1(k)). To prevent thermal shock of the substrate, the temperature is ramped up and down at a slow rate. During ramping O_2 was flowed to ensure atmospheric gases do not reach the substrate while it is above room temperature.

3. Design and simulation

An array of optical ring resonators based on a rib waveguide etched into a slab with perforations along the full length are designed with various waveguide-ring coupling gaps and waveguide widths. These include five columns of eight resonators with 40 μm radius of each ring, where each resonator is coupled to a single mode bus waveguide with a coupling gap that varies from 100 to 400 nm in steps of 50 nm. The optimal waveguide dimensions are determined by finite element method simulations in COMSOL Multiphysics based on a maximum etch depth of 350 nm, and a sidewall angle of 75.6°. The waveguide dimensions are chosen to provide high confinement with minimal bending loss and single TE-mode operation with an effective refractive index (n_{eff}) of 2.04. A slab height of 100 nm is found to offer maximum mode confinement while ensuring adequate mechanical support for the structure. As an example, the bus waveguide structure is depicted in Fig. 2(a), which has a top waveguide width of 580 nm. The ring resonators have various waveguide widths featuring a top widths 0.8, 1, 1.5, 1.8 and 2 μm for each column. Uniform pitch VGCs are designed with a partial etch depth of 180 nm, an etch angle of 75.6°, a top

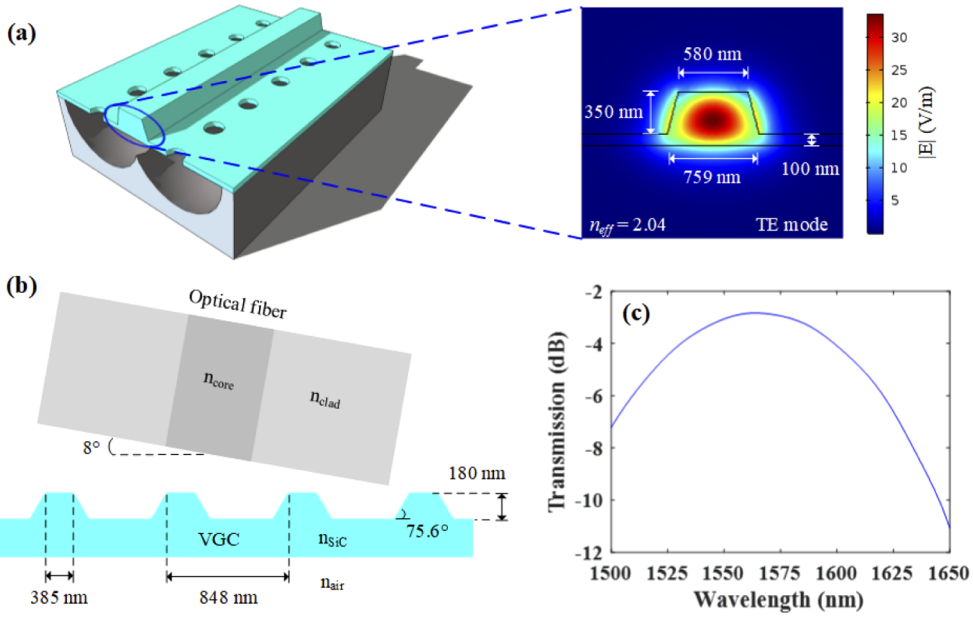

Fig. 2. Designs of the optical waveguide and vertical grating coupler (VGC). (a) Schematic representation of the etched waveguide structure showing the undercut areas and cross section and normalized electric field magnitude of the fundamental (TE) mode of the single mode waveguide. (b) VGC design showing the dimensions to achieve optimal coupling efficiency and bandwidth. (c) Simulated transmission of the VGC showing a maximum coupling loss of 3 dB.

Optics EXPRESS

tooth width of 385 nm, a period of 848 nm and a fill factor of 0.45, as shown in Fig. 2(b), which are optimized for maximum optical bandwidth and coupling efficiency for a 8° tilted single mode optical fiber injecting TE-polarized light. Our finite difference time domain (FDTD) simulations predict a −3 dB optical bandwidth of approximate 109 nm (Fig. 2(c)) by using refraction indices of $n_{sic} = 2.55$, $n_{air} = 1$, $n_{core} = 1.45$ and $n_{clad} = 1.44$, of 3C-SiC, air, the fiber core and cladding respectively.

4. Device characterization

The fabricated devices are characterized using optical microscopy, SEM, AFM, XRD and XPS before and after thermal annealing. An optical microscope image of a single ring structure is shown in Fig. 3(a). The green translucent area surrounding the waveguides is a result of the undercut area, which is visible through the thin SiC slab. SEM images with 30° tilt of the bus waveguide and ring resonator coupling region before and after thermal annealing are shown in Fig. 3(b). A clear reduction in sidewall roughness of the waveguides is observed after the annealing step. The AFM (Asylum Research MFP-3D) is used to measure the surface roughness of the waveguides. The results are shown in Figs. 3(c) and 3(d). The RMS value of the measured top waveguide surface roughness prior to annealing is 2.4 nm for a 2 µm × 0.5 µm area, consistent with that expected from the wafer thinning process and close to the polishing roughness of CMP. The RMS roughness is reduced to approximately 1.7 nm after annealing measured in the same area. Although we could not directly measure the sidewall roughness using the AFM tip available, we could infer a similar reduction in roughness from the oblique interaction of the AFM tip with the edges of the waveguide. Thermal annealing of SiC in an oxygen atmosphere is known to

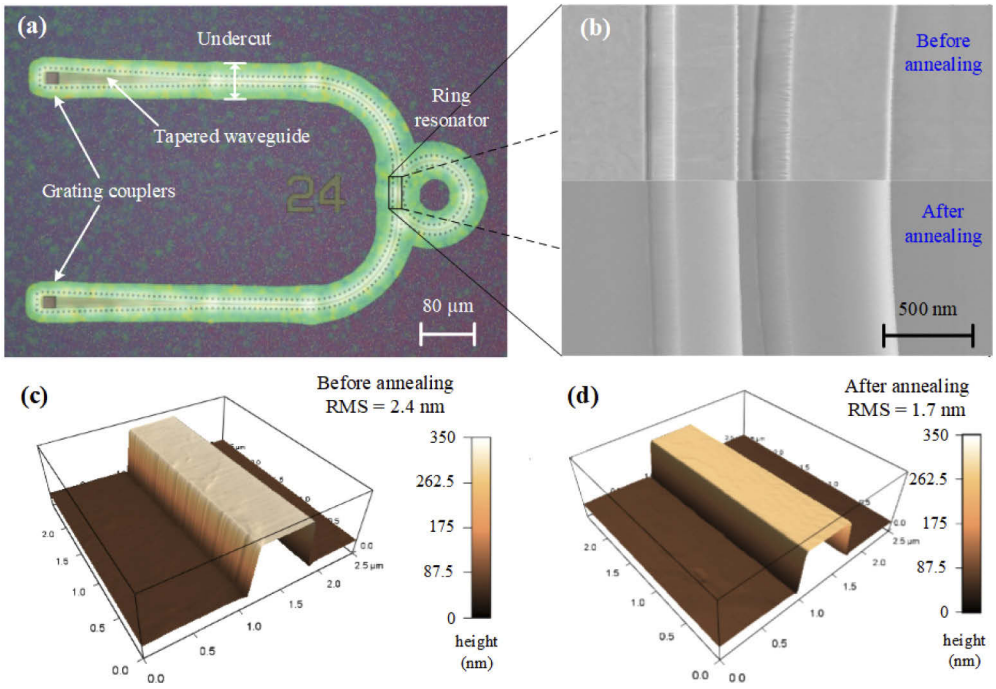

Fig. 3. Metrology of the fabricated optical waveguides. (a) Optical micrograph of the device (b) scanning electron micrograph of the coupling region between the bus waveguide and ring waveguide with a 40 um radius, 0.8 um waveguide width and 100 nm coupling gap. (c) AFM of the waveguide surface before (d) and after annealing.

Optics EXPRESS

oxidize the surface layer at relatively low rates [46]. Our measurements suggest that oxidation of 3C-SiC leads to smoothing of the waveguides in a similar manner to that of Si waveguides [47,48]. Oxidation induced smoothing is caused by convex points on the waveguide sidewall being oxidized at a higher rate than concave points due to a greater oxidant supply rate at the convex parts of the surface. This effect results in a reduction in the amount of scattered light at the SiO_2/SiC-air interface compared to the SiC-air interface of the non-annealed chip.

It is expected that thermal annealing will increase the crystal grain size and hence reduce magnitude of optical scattering losses at the grain boundaries or reduce the impact of defect-induced absorption from dangling bonds at the boundaries [45,49]. We use XRD to determine the impact of annealing on the overall crystallinity of 3C-SiC at the device layer. Diffractions at angles of 41.83° and 90.37° from the normal correspond to 3C-SiC(200) and 3C-SiC(400) respectively consistent with the wafer orientation of <100> [50–52]. The diffraction spectra before annealing as shown in Fig. 4(a) are found to have wide FWHM of 0.477° and 0.716° indicative of polycrystallinity. After annealing, the positions of the diffraction spectra shown in Fig. 4(b) remain constant, indicative of an intact 3C structure [53]. However, a reduction of FWHM 44.8% and 18.3% of the 3C-SiC(200) and 3C-SiC(400) diffraction intensities, indicates an increase in average grain size.

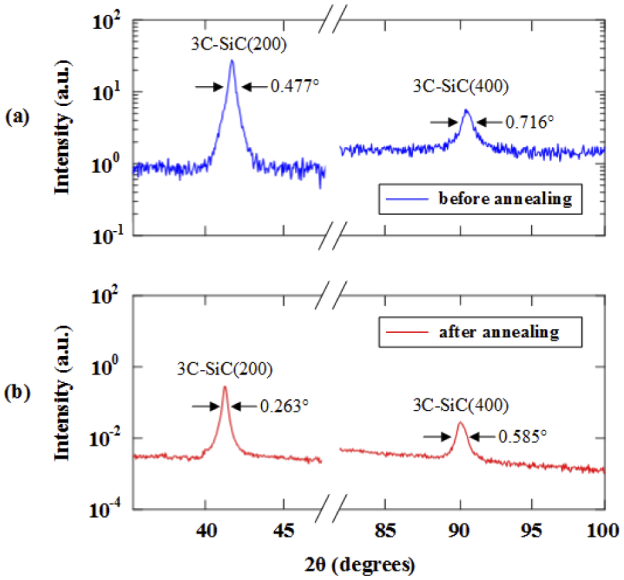

Fig. 4. X-ray diffraction measurement of the SiC thin film showing a narrowing of the 3C-SiC(200) and SiC(400) peaks from annealing. (a) Before annealing. (b) After annealing for 2 hours at 1100 °C in O_2.

Next, we conduct a surface analysis using an XPS (Thermo Scientific K-alpha) to confirm the growth of SiO_2 on the SiC surface after thermal annealing, where the XPS could survey the atoms of elements in top 10 nm. The XPS measurement of the chip prior to annealing is shown in Fig. 5(a) that indicates the following elements and associated electronic configurations: O1s, C1s, Si2s and Si2p. The O1s and Si2s/Si2p intensities represent the presence of SiO_2 likely due to a native oxide layer on the SiC surface while Si2s/Si2p and C1s confirms the presence of SiC. However, no carbon is detected after annealing while the density of oxygen increases by more than one order of magnitude, with silicon density unchanged as shown in Fig. 5(b), which indicates an oxide thickness of greater than 10 nm. Our results strongly suggest the formation of

Optics EXPRESS

a SiO_2 layer on the SiC due to thermal oxidization in support of our observations from SEM and AFM measurements.

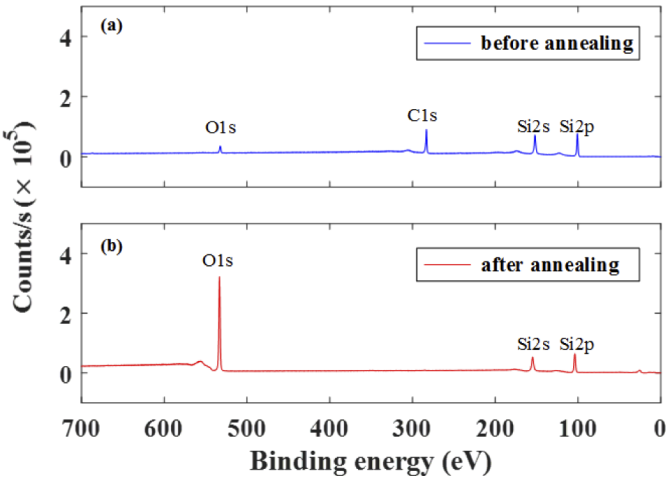

Fig. 5. X-ray photoelectron spectroscopy of the SiC surface indicating a change in surface composition after annealing. (a) Before annealing. (b) After annealing in O_2 at 1100 °C for 2 hours.

5. Optical characterization

Critically, we determine the optical quality factor of the fabricated ring resonators prior to and subsequently after annealing to determine any impact of annealing on the waveguide propagation loss. Light is coupled into, and out of, each ring resonator via the VGCs using a two channel fiber array featuring 254 μm fiber pitch and 8° polishing angle which minimize back reflections. The spectral response of each resonator is obtained by varying the wavelength of light from 1500 nm to 1550 nm using a grating-stabilized continuous-wave laser and capturing the output of the resonator using a photodiode. The measured optical coupling loss of each VGC is approximately 5 dB. Moreover, a 97.4% yield of VGCs is achieved across 40 devices on chip. A 50 nm blue-shift of the spectral envelope of the VGC is observed after annealing. The corresponding oxide thickness is determined to be 40 nm using FDTD simulation in Lumerical. The optical spectrum of a ring resonator featuring a waveguide width of 2 μm and a radius of 40 μm is depicted in Fig. 6(a). The comparatively large waveguide width is chosen to reduce the impact of sidewall scattering losses to the inferred Q-factor such that a closer value to intrinsic material limited loss can be inferred. We find that the ring resonator supports three spatial modes and features a free spectral range (FSR) of 3.35 nm (Fig. 6(a)) prior to annealing. Two additional higher-order modes appeared after annealing the resonators are due to a reduction in loss which enables poorly-confined modes to propagate. The FSR reduces slightly to 3.12 nm however the overall extinction ratio goes up indicating conditions closer to critical coupling than prior to annealing. In Fig. 6(b), the linewidth of mode 3 is compared before and after annealing using Lorentz fitting. Note the power variation induced by the slope of the VGC is less than 0.03 dB that is negligible in the fitting. The intrinsic Q factor (Q_i) for undercoupled resonators is given by

$$Q_i = \frac{2Q_L}{1 + \sqrt{T}} \tag{1}$$

where Q_L is the loaded quality factor and T is the on-resonance transmission. We compare the intrinsic Q factor to remove the loading effects of varied coupling gaps and waveguide

Optics EXPRESS

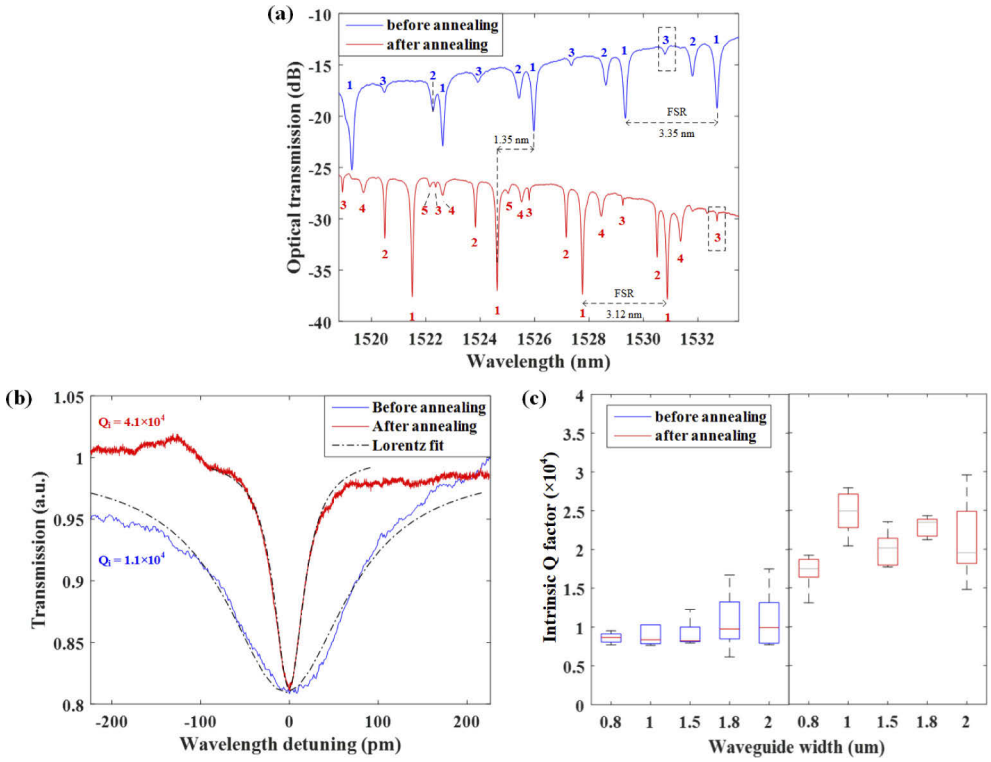

Fig. 6. Analysis of impact on optical Q factor by thermal annealing. (a) Ring resonator transmission spectrum for ring radius of 40 μm showing 3 resonant modes before annealing and 5 resonant modes after annealing. A blue shift of 1.35 nm is due to annealing. (b) Lorentzian fit of resonance of mode three before (1530.5 nm) and after annealing (1532.7 nm) indicates a significant reduction in linewidth. (c) Box plot of intrinsic Q factors of the fundamental TE mode (mode 1) of each waveguide width before and after annealing showing the median (red line), bottom and top edge of the box (25th and 75th percentiles respectively), whiskers showing the absolute minimum and maximum measured Q factors of 8 resonators per box.

confinement factors. The ring resonators are assumed to be operating in the under-coupled regime, giving a lower-limit to the estimated intrinsic Q factor. For fair comparison, the same spatio-longitudinal mode that features the highest intrinsic Q factor when compared to all other longitudinal modes was compared to that before and after annealing. A 146 pm line-width was measured before annealing, corresponding to an intrinsic Q factor of 1.1×10^4, which indicates linear propagation losses of around 24 dB/cm. The line width is reduced to 39 pm after annealing, corresponding to an intrinsic Q factor of over 4.1×10^4, which is the result of an estimated linear propagation loss of 7 dB/cm, a 373% improvement. This improvement in propagation losses is not limited to one device, as loaded Q factors and extinction ratios increased universally across all of the measured devices. The statistical significance is illustrated in Fig. 6(c) that summarizes the intrinsic Q factors of the fundamental TE mode (mode 1) for all five columns of ring resonators with different waveguide widths. The average median intrinsic Q factor before annealing is 0.9×10^4 across all waveguide widths, with a minimum of 0.61×10^4 and maximum of 1.7×10^4. After annealing the average median intrinsic Q factor increased to 2.1×10^4 with a minimum and maximum Q factor of 1.3×10^4 and 3.0×10^4, respectively, producing a 250% increase in average median intrinsic Q factor. No overlap is observed between interquartile ranges of the measured

Optics EXPRESS

Q factor before and after annealing, indicating a high statistical significance. The increase in Q factor is consistent with the reduction in surface roughness and improvement in crystallinity that are indicated from AFM, XRD and XPS measurements. Models which predict propagation losses based on surface roughness also indicate that reduced roughness from 2.4 nm to 1.7 nm can lower optical propagation losses [54,55]. We also postulate that the formation of SiO_2 on the waveguides may aid in the reduction of crystal defect density particularly underneath the waveguide where it is highest [26] and oxidation can occur. We believe the oxidation growth on the SiC surface can replace shallow defects in accordance to the thickness of the oxide which help to eliminate some of the scattering induced losses from the crystal defects.

Finally, thermo-optic measurements are performed on one of the fabricated ring resonators prior to and subsequently after annealing to determine any potential impact on the thermal properties of SiC, a distinguishing feature of this crystal which can be used for resonance wavelength tuning with micro heaters [56]. The temperature of the sample is controlled with a variable hot plate and resonance spectra is recorded at regular intervals of 4 K from 298 to 473 K. Slight resonance detuning is observed with annealing as discussed in Section 4, and a red shift accompanies increasing temperature as shown in Fig. 7(a). The temperature-induced resonance detuning is converted into a variation of the refractive index (dn/dT) given by

$$\frac{dn}{dT} = \frac{n_{sic}}{\lambda_0}\frac{d\lambda}{dT} \tag{2}$$

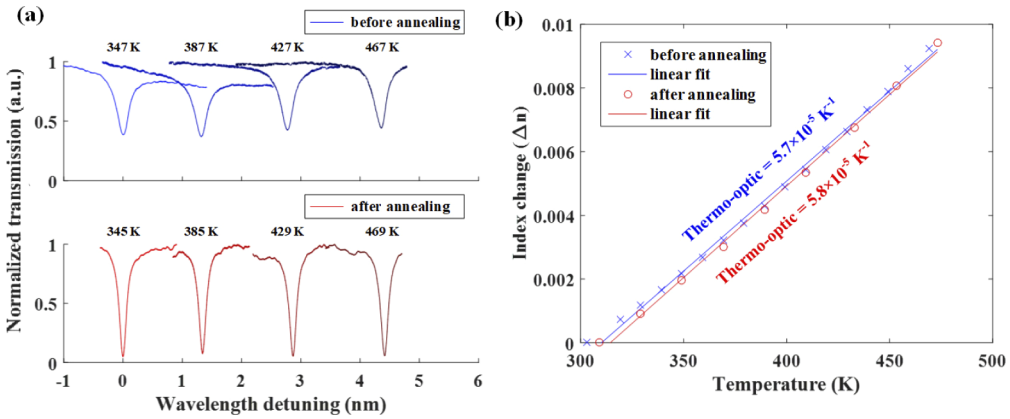

Fig. 7. Thermo-optic measurements of the fabricated ring resonators before and after annealing. (a) Wavelength detuning with increasing temperature showing a red shift. (b) Refractive index change as a function of temperature used to determine the thermo-optic coefficient.

where λ is the wavelength, n is the refractive index, T is temperature,, λ_0 is the resonance wavelength, and the refractive index of SiC (n_{sic}) is set as 2.55 for the wavelength range. Figure 7(b) shows the estimated refractive index change as a function of temperature. By using the linear curve fitting, the thermo-optic coefficients before and after annealing are obtained as 5.7×10^{-5} K^{-1} and 5.8×10^{-5} K^{-1} respectively, which is only 1.7% variation. Its magnitude is similar to the thermo-optic coefficient of bulk 3C-SiC [13] confirming our thermal annealing approach does not alter the desirable thermal properties of 3C-SiC aside from the desired effects of reduction in waveguide loss.

6. Conclusion

Despite the excellent optical properties of 3C-SiC, inevitable crystal growth defects hinder its development for low loss suspended integrated optical devices. We develop a new anisotropic

Optics EXPRESS

etch recipe to achieve low waveguide roughness of 2.4 nm in 3C-SiC with waveguide top-width dimension of 580 nm. With thermal annealing in oxygen atmosphere we reduce the RMS roughness to 1.7 nm, while also lowering the defect density through grain size enlargement and surface oxidation. This results in an overall improvement to crystallinity of the 3C-SiC film which is supported by XRD and XPS analysis. These new techniques enable us to achieve a significant reduction in linear optical propagation losses from 24 dB/cm to 7 dB/cm, corresponding to an optical Q factor of over 41,000 in a suspended waveguide coupled optical ring resonator. Furthermore, by temperature-dependent measurements of the fabricated ring resonators, we measure a low thermo-optic coefficient of 5.8×10^{-5} K^{-1} consistent with that of bulk SiC confirming that thermal annealing does not impact the desirable thermal properties of 3C-SiC. Overall, we demonstrate that thermal annealing is an effective method for improving waveguide losses in suspended 3C-SiC photonic structures. Our work paves the way toward low loss suspended devices in 3C-SiC. These devices are important for optomechanical and surface acoustic devices that could utilize the excellent mechanical properties of this platform. Finally, we note that this work may be relevant to other SiC platforms such as SiCOI and polytypes such as 4H, 6H and amorphous SiC.

Funding

University of Sydney (Sydney Research Accelerator Fellowship, Harvard University Mobility Scheme, Research Training Program Scholarship); Natural Sciences and Engineering Research Council of Canada (INQNET Research Program); U.S. Department of Energy (DE-SC0019219).

Acknowledgments

This work was carried out at the Harvard Center for Nanoscale Systems (CNS), a member of the National Nanotechnology Infrastructure Network (NNIN). The authors would like to thank Guixiong Zhong at CNS for carrying out XRD measurements, Jianfu Wang, Liwei Li and Michael Collins from the University of Sydney for their help with optical waveguides and annealing techniques.

Disclosures

The authors declare that there are no conflicts of interest related to this article.

References

1. M. Glick, L. C. Kimmerling, and R. C. Pfahl, "A Roadmap for Integrated Photonics," Opt. Photonics News **29**(3), 36 (2018).
2. D. Thomson, A. Zilkie, J. E. Bowers, T. Komljenovic, G. T. Reed, L. Vivien, D. Marris-Morini, E. Cassan, L. Virot, J. M. Fédéli, J. M. Hartmann, J. H. Schmid, D. X. Xu, F. Boeuf, P. O'Brien, G. Z. Mashanovich, and M. Nedeljkovic, "Roadmap on silicon photonics," J. Opt. **18**(7), 073003 (2016).
3. I. J. Wu and G. Y. Guo, "Second-harmonic generation and linear electro-optical coefficients of SiC polytypes and nanotubes," Phys. Rev. B **78**(3), 035447 (2008).
4. J. Cardenas, M. Yu, Y. Okawachi, C. B. Poitras, R. K. W. Lau, A. Dutt, A. L. Gaeta, and M. Lipson, "Optical nonlinearities in high-confinement silicon carbide waveguides," Opt. Lett. **40**(17), 4138 (2015).
5. F. Martini and A. Politi, "Four wave mixing in 3C SiC ring resonators," Appl. Phys. Lett. **112**(25), 251110 (2018).
6. D. M. Lukin, C. Dory, M. A. Guidry, K. Y. Yang, S. D. Mishra, R. Trivedi, M. Radulaski, S. Sun, D. Vercruysse, G. H. Ahn, and J. Vučković, "4H-silicon-carbide-on-insulator for integrated quantum and nonlinear photonics," Nat. Photonics (2019).
7. F. Nabki, T. A. Dusatko, S. Vengallatore, and M. N. El-Gamal, "Low-stress CMOS-compatible silicon carbide surface-micromachining technology-part I: Process development and characterization," J. Microelectromech. Syst. **20**(3), 720–729 (2011).
8. L. S. Pakula, H. Yang, H. T. M. Pham, P. J. French, and P. M. Sarro, "Fabrication of a CMOS compatible pressure sensor for harsh environments," J. Micromech. Microeng. **14**(11), 1478–1483 (2004).
9. F. Schäffl, "Properties of advanced semiconductor materials : GaN, AlN, InN, BN, SiC, SiGe," John Wiley Sons Inc New York 149 (2001).

Optics EXPRESS

10. F. De Leonardis, R. A. Soref, and V. M. N. Passaro, "Dispersion of nonresonant third-order nonlinearities in Silicon Carbide," Sci. Rep. **7**(1), 40924 (2017).
11. W. Daves, A. Krauss, N. Behnel, V. Häublein, A. Bauer, and L. Frey, "Amorphous silicon carbide thin films (a-SiC:H) deposited by plasma-enhanced chemical vapor deposition as protective coatings for harsh environment applications," Thin Solid Films **519**(18), 5892–5898 (2011).
12. W. J. Choyke, R. F. Farich, and R. A. Hoffman, "SiC, a new material for mirrors 1: High power lasers; 2: VUV applications," Appl. Opt. **15**(9), 2006 (1976).
13. X. Lu, J. Y. Lee, P. X.-L. Feng, and Q. Lin, "Silicon carbide microdisk resonator," Opt. Lett. **38**(8), 1304–1306 (2013).
14. K. M. Jackson, J. Dunning, C. A. Zorman, M. Mehregany, and W. N. Sharpe, "Mechanical properties of epitaxial 3C silicon carbide thin films," J. Microelectromech. Syst. **14**(4), 664–672 (2005).
15. M. Radulaski, T. M. Babinec, K. Müller, K. G. Lagoudakis, J. L. Zhang, S. Buckley, Y. A. Kelaita, K. Alassaad, G. Ferro, and J. Vučković, "Visible Photoluminescence from Cubic (3C) Silicon Carbide Microdisks Coupled to High Quality Whispering Gallery Modes," ACS Photonics **2**(1), 14–19 (2015).
16. S. Castelletto, B. C. Johnson, V. Ivády, N. Stavrias, T. Umeda, A. Gali, and T. Ohshima, "A silicon carbide room-temperature single-photon source," Nat. Mater. **13**(2), 151–156 (2014).
17. I. Aharonovich, D. Englund, and M. Toth, "Solid-state single-photon emitters," Nat. Photonics **10**(10), 631–641 (2016).
18. F. Fuchs, B. Stender, M. Trupke, D. Simin, J. Pflaum, V. Dyakonov, and G. V. Astakhov, "Engineering near-infrared single-photon emitters with optically active spins in ultrapure silicon carbide," Nat. Commun. **6**(1), 7578 (2015).
19. A. Lohrmann, N. Iwamoto, Z. Bodrog, S. Castelletto, T. Ohshima, T. J. Karle, A. Gali, S. Prawer, J. C. McCallum, and B. C. Johnson, "Single-photon emitting diode in silicon carbide," Nat. Commun. **6**(1), 7783 (2015).
20. B. Lienhard, T. Schröder, S. Mouradian, F. Dolde, T. T. Tran, I. Aharonovich, and D. Englund, "Bright and photostable single-photon emitter in silicon carbide," Optica **3**(7), 768 (2016).
21. H. Zhuang, L. Zhang, T. Staedler, and X. Jiang, "Low Temperature Hetero-Epitaxial Growth of 3C-SiC Films on Si Utilizing Microwave Plasma CVD," Chem. Vap. Deposition **19**(1-3), 29–37 (2013).
22. A. Vonsovici, G. T. Reed, and A. G. R. Evans, "β-SiC-on insulator waveguide structures for modulators and sensor systems," Mater. Sci. Semicond. Process. **3**(5-6), 367–374 (2000).
23. X. Tang, K. G. Irvine, D. Zhang, and M. G. Spencer, "Linear electro-optic effect in cubic silicon carbide," Appl. Phys. Lett. **59**(16), 1938–1939 (1991).
24. P. S. Kuo, J. Bravo-Abad, and G. S. Solomon, "Second-harmonic generation using -quasi-phasematching in a GaAs whispering-gallery-mode microcavity," Nat. Commun. **5**(1), 3109 (2014).
25. Z. Yang, P. Chak, A. D. Bristow, H. M. van Driel, R. Iyer, J. S. Aitchison, A. L. Smirl, and J. E. Sipe, "Enhanced second-harmonic generation in AlGaAs microring resonators," Opt. Lett. **32**(7), 826 (2007).
26. T. Fan, H. Moradinejad, X. Wu, A. A. Eftekhar, and A. Adibi, "High-Q integrated photonic microresonators on 3C-SiC-on-insulator (SiCOI) platform," Opt. Express **26**(20), 25814 (2018).
27. Y. Zheng, M. Pu, A. Yi, B. Chang, T. You, K. Huang, A. N. Kamel, M. R. Henriksen, A. A. Jørgensen, X. Ou, and H. Ou, "High-quality factor, high-confinement microring resonators in 4H-silicon carbide-on-insulator," Opt. Express **27**(9), 13053 (2019).
28. D. Lukin, C. Dory, M. Radulaski, S. Sun, S. D. Mishra, M. Guidry, D. Vercruysse, and J. Vučković, "4H-SiC-on-Insulator Platform for Quantum Photonics," in *Conference on Lasers and Electro-Optics* (OSA, 2019), p. SM2F.6.
29. X. Lu, J. Y. Lee, P. X.-L. Feng, and Q. Lin, "High Q silicon carbide microdisk resonator," Appl. Phys. Lett. **104**(18), 181103 (2014).
30. T. Fan, X. Wu, Ali A. Eftekhar, and A. Adibi, "Record-High-Q Microresonators from 650 nm to 1550 nm Wavelengths on a 3C-SiC-on-Insulator Platform," in *CLEO: Science and Innovations* (Optical Society of America, 2019), p. STh1H.5.
31. A. P. Magyar, D. Bracher, J. C. Lee, I. Aharonovich, and E. L. Hu, "High quality SiC microdisk resonators fabricated from monolithic epilayer wafers," Appl. Phys. Lett. **104**(5), 051109 (2014).
32. M. Radulaski, T. M. Babinec, S. Buckley, A. Rundquist, J. Provine, K. Alassaad, G. Ferro, and J. Vučković, "Photonic crystal cavities in cubic (3C) polytype silicon carbide films," Opt. Express **21**(26), 32623 (2013).
33. D. O. Bracher and E. L. Hu, "Fabrication of High- Q Nanobeam Photonic Crystals in Epitaxially Grown 4H-SiC," Nano Lett. **15**(9), 6202–6207 (2015).
34. F. Martini and A. Politi, "Linear integrated optics in 3C silicon carbide," Opt. Express **25**(10), 10735 (2017).
35. B.-S. Song, T. Asano, S. Jeon, H. Kim, C. Chen, D. D. Kang, and S. Noda, "Ultrahigh-Q photonic crystal nanocavities based on 4H silicon carbide," Optica **6**(8), 991 (2019).
36. B. S. Song, S. Jeon, H. Kim, D. D. Kang, T. Asano, and S. Noda, "High-Q-factor nanobeam photonic crystal cavities in bulk silicon carbide," Appl. Phys. Lett. **113**(23), 231106 (2018).
37. M. Ziaei-Moayyed, M. F. Su, C. Reinke, I. F. El-Kady, and R. H. Olsson, "Silicon carbide phononic crystal cavities for micromechanical resonators," in *2011 IEEE 24th International Conference on Micro Electro Mechanical Systems* (IEEE, 2011), pp. 1377–1381.

Optics EXPRESS

38. A. Lohrmann, T. J. Karle, V. K. Sewani, A. Laucht, M. Bosi, M. Negri, S. Castelletto, S. Prawer, J. C. McCallum, and B. C. Johnson, "Integration of Single-Photon Emitters into 3C-SiC Microdisk Resonators," ACS Photonics **4**(3), 462–468 (2017).
39. J. Vuckovic, "Connecting quantum systems through optimized photonics (Conference Presentation)," in *Quantum Nanophotonic Materials, Devices, and Systems 2019*, M. Agio, C. Soci, and M. T. Sheldon, eds. (SPIE, 2019), p. 2.
40. S. J. Whiteley, G. Wolfowicz, C. P. Anderson, A. Bourassa, H. Ma, M. Ye, G. Koolstra, K. J. Satzinger, M. V. Holt, F. J. Heremans, A. N. Cleland, D. I. Schuster, G. Galli, and D. D. Awschalom, "Spin–phonon interactions in silicon carbide addressed by Gaussian acoustics," Nat. Phys. **15**(5), 490–495 (2019).
41. D. N. Talwar and J. C. Sherbondy, "Thermal expansion coefficient of 3C–SiC," Appl. Phys. Lett. **67**(22), 3301–3303 (1995).
42. Y. Okada and Y. Tokumaru, "Precise determination of lattice parameter and thermal expansion coefficient of silicon between 300 and 1500 K," J. Appl. Phys. **56**(2), 314–320 (1984).
43. S. Uekusa and T. Goto, "Photoluminescence From Er ¯ Implanted 4 h And 6h-SiC," Mater. Res. Soc. Symp. Proc. **692**, H6.13.1 (2001).
44. J. Cardenas, M. Zhang, C. T. Phare, S. Y. Shah, C. B. Poitras, B. Guha, and M. Lipson, "High Q SiC microresonators," Opt. Express **21**(14), 16882 (2013).
45. M. Bosi, G. Attolini, M. Negri, C. Ferrari, E. Buffagni, C. Frigeri, M. Calicchio, B. Pécz, F. Riesz, I. Cora, Z. Osváth, L. Jiang, and G. Borionetti, "Defect structure and strain reduction of 3C-SiC/Si layers obtained with the use of a buffer layer and methyltrichlorosilane addition," CrystEngComm **18**(15), 2770–2779 (2016).
46. C. D. Fung and J. J. Kopanski, "Thermal oxidation of 3C silicon carbide single-crystal layers on silicon," Appl. Phys. Lett. **45**(7), 757–759 (1984).
47. J. Takahashi, T. Tsuchizawa, T. Watanabe, and S. Itabashi, "Oxidation-induced improvement in the sidewall morphology and cross-sectional profile of silicon wire waveguides," J. Vac. Sci. Technol., B: Microelectron. Process. Phenom. **22**(5), 2522 (2004).
48. K. K. Lee, D. R. Lim, L. C. Kimerling, J. Shin, and F. Cerrina, "Fabrication of ultralow-loss Si/SiO_2 waveguides by roughness reduction," Opt. Lett. **26**(23), 1888 (2001).
49. Y. Shoji, K. Nakanishi, Y. Sakakibara, K. Kintaka, H. Kawashima, M. Mori, and T. Kamei, "Hydrogenated Amorphous Silicon Carbide Optical Waveguide for Telecommunication Wavelength Applications," Appl. Phys. Express **3**(12), 122201 (2010).
50. C. Wang, N. Huang, H. Zhuang, Z. Zhai, B. Yang, L. Liu, and X. Jiang, "Growth of large-scale heteroepitaxial 3C-SiC films and nanosheets on silicon substrates by microwave plasma enhanced CVD at higher powers," Surf. Coat. Technol. **299**, 96–103 (2016).
51. A. R. Md Foisal, H.-P. Phan, T. Dinh, T.-K. Nguyen, N.-T. Nguyen, and D. V. Dao, "A rapid and cost-effective metallization technique for 3C–SiC MEMS using direct wire bonding," RSC Adv. **8**(28), 15310–15314 (2018).
52. M. R. Sardela, "X-Ray Diffraction and Reflectivity," 1–41 (2014).
53. Y. K. Sharma, F. Li, C. A. Fisher, M. R. Jennings, D. Hamilton, S. M. Thomas, A. Pérez-Tomás, and P. A. Mawby, "Fabrication of 3C-SiC MOS Capacitors Using High-Temperature Oxidation," Mater. Sci. Forum **821-823**, 464–467 (2015).
54. Y. A. Vlasov and S. J. McNab, "Losses in single-mode silicon-on-insulator strip waveguides and bends," Opt. Express **12**(8), 1622 (2004).
55. K. K. Lee, D. R. Lim, H. C. Luan, A. Agarwal, J. Foresi, and L. C. Kimerling, "Effect of size and roughness on light transmission in a Si/SiO2waveguide: Experiments and model," Appl. Phys. Lett. **77**(11), 1617–1619 (2000).
56. X. Wu, T. Fan, A. A. Eftekhar, and A. Adibi, "High-Q microresonators integrated with microheaters on a 3C-SiC-on-insulator platform," Opt. Lett. **44**(20), 4941 (2019).